Achieving 23.83% conversion efficiency in silicon heterojunction solar cell with ultra-thin MoO_x hole collector layer via tailoring (i)a-Si:H/MoO_x interface

Cao, Liqi; Procel, Paul; Alcañiz, Alba; Yan, Jin; Tichelaar, Frans; Özkol, Engin; Zhao, Yifeng; Han, Can; Yang, Guangtao; Yao, Zhirong

DOI
10.1002/pip.3638

Publication date
2022

Document Version
Final published version

Published in
Progress in Photovoltaics: research and applications

Citation (APA)
Cao, L., Procel, P., Alcañiz, A., Yan, J., Tichelaar, F., Özkol, E., Zhao, Y., Han, C., Yang, G., Yao, Z., Zeman, M., Santbergen, R., Mazzarella, L., & Isabella, O. (2022). Achieving 23.83% conversion efficiency in silicon heterojunction solar cell with ultra-thin MoO_x hole collector layer via tailoring (i)a-Si:H/MoO_x interface. *Progress in Photovoltaics: research and applications*, *31*(12), 1245-1254. https://doi.org/10.1002/pip.3638

Received: 29 June 2022 | Revised: 20 September 2022 | Accepted: 4 October 2022
DOI: 10.1002/pip.3638

SPECIAL ISSUE ARTICLE

PROGRESS IN PHOTOVOLTAICS WILEY

Achieving 23.83% conversion efficiency in silicon heterojunction solar cell with ultra-thin MoO_x hole collector layer via tailoring (*i*)a-Si:H/MoO_x interface

Liqi Cao[1] | Paul Procel[1,2] | Alba Alcañiz[1] | Jin Yan[1] | Frans Tichelaar[3] | Engin Özkol[1] | Yifeng Zhao[1] | Can Han[1] | Guangtao Yang[1] | Zhirong Yao[1] | Miro Zeman[1] | Rudi Santbergen[1] | Luana Mazzarella[1] | Olindo Isabella[1]

[1]Photovoltaic Materials and Devices Group, Delft University of Technology, Delft, The Netherlands

[2]Institute of Micro and Nanoelectronics, San Francisco de Quito University, Quito, Ecuador

[3]Kavli Institute of Technology, Quantum Nanoscience, Delft University of Technology, Delft, The Netherlands

Correspondence
Liqi Cao, Photovoltaic Materials and Devices Group, Delft University of Technology, Delft, The Netherlands.
Email: l.cao-3@tudelft.nl

Funding information
Topsector Energie of the Dutch Ministry of Economic Affairs and Climate Policy; China Scholarship Council, Grant/Award Number: 202006740021

Abstract

Thin films of transition metal oxides such as molybdenum oxide (MoO_x) are attractive for application in silicon heterojunction solar cells for their potential to yield large short-circuit current density. However, full control of electrical properties of thin MoO_x layers must be mastered to obtain an efficient hole collector. Here, we show that the key to control the MoO_x layer quality is the interface between the MoO_x and the hydrogenated intrinsic amorphous silicon passivation layer underneath. By means of ab initio modelling, we demonstrate a dipole at such interface and study its minimization in terms of work function variation to enable high performance hole transport. We apply this knowledge to experimentally tailor the oxygen content in MoO_x by plasma treatments (PTs). PTs act as a barrier to oxygen diffusion/reaction and result in optimal electrical properties of the MoO_x hole collector. With this approach, we can thin down the MoO_x thickness to 1.7 nm and demonstrate short-circuit current density well above 40 mA/cm^2 and a champion device exhibiting 23.83% conversion efficiency.

KEYWORDS

dipole, fundamental study, industrial approach, numerical modelling, plasma treatment, silicon heterojunction solar cells, tailoring MoO_x, ultra-thin MoO_x

1 | INTRODUCTION

Silicon-based solar cells dominate the market of photovoltaics, which hold the highest potential for green electricity production.[1,2] A front/back-contacted architecture combined with silicon heterojunction (SHJ) concept realized a world record efficiency of 26.5%.[3] However, conventional silicon-based doped layers, which work as carrier-selective transport layers, are not ideally transparent.[4] Furthermore, misalignment of the band structure at doped a-Si/c-Si interface and doped a-Si/transparent conductive oxide (TCO) interface translates into fill factor losses.[5,6]

Transition metal oxide (TMO) materials have been investigated to circumvent this fundamental limitation.[7–12] The interest in TMO thin

---

Liqi Cao and Paul Procel contribute equally to this work.

films stems mainly from their wide-range tunable work function (WF), electronic properties, and good transparency, all of which are important for application in SHJ solar cells.[13,14] Molybdenum oxide (MoO_x) as one of the most promising hole transport layers (HTL) has been well examined.[15–19] In this respect, different processing methods have been investigated to exploit the potential of MoO_x layers. For instance, MoO_x films have been produced by a solution process using organic precursors followed by thermal treatment,[20] atomic layer deposition,[21–23] and thermal evaporation.[23,24] Furthermore, SHJ solar cells using MoO_x have achieved above 22% efficiency[16,19] and, so far, a record performance of 23.5% with the potential for further improvements.[25]

However, several issues occurring at a-Si:H/MoO_x interface have been reported.[26,27] Most prominently, the formation of a thin SiO_x layer during the deposition of MoO_x has been shown in.[16,18,25,28] Some research reported that the electronic properties of MoO_x are regulated by its oxygen content[29–31] and by the interfacial condition with its growth substrate. Controlling these aspects is thus crucial for the effective application of MoO_x in high-efficiency solar cells. In particular, several works attempted to limit the reaction between the MoO_x and the intrinsic hydrogenated amorphous silicon, (*i*)a-Si:H, underneath by annealing[25] and by pre-growth of a SiO_x layer.[32,33] Specifically, a surface treatment on the (*i*)a-Si:H layer before MoO_x deposition improves solar cell performance.[19] Nevertheless, the fundamental knowledge of the phenomena occurring at the (*i*)a-Si:H/MoO_x interface and its application for achieving efficient solar cells devices is not well understood yet.

This work presents a complete study of SHJ solar cells based on MoO_x hole collector from fundamental theory up to device-level integration. We first present a theoretical framework of MoO_x properties depending on silicon-based substrates (i.e., (*i*)a-Si:H). Accordingly, we investigate an industry-appealing plasma treatment method to control the growth of high quality MoO_x thin films by achieving an optimal oxygen content. Then, we evaluate the transport properties of the whole hole contact stack by measuring its contact resistivity. Finally, we showcase high-efficiency heterojunction solar cells with ultra-thin MoO_x films, achieving short-circuit current density equal to 40.2 mA/cm^2 and, in the same device, a champion conversion efficiency of 23.83%.

2 | METHODOLOGY

2.1 | Experimental

Figure 1 shows the flow chart for the manufacturing of MoO_x-based SHJ solar cells. The samples were prepared using 4-in. double-side polished n-type FZ wafers with <100> orientation. The resistivity and thickness of the wafers are 3 ± 2 Ω cm and 280 ± 20 μm, respectively. Wafer texturing process was conducted in a TMAH solution with ALKA-TEX as an additive.[34] Next, the wafers were cleaned using wet-chemical cleaning and dipping them in 0.55% hydrogen fluoride (HF) for 5 min.[34] Afterwards, the wafers were loaded into a multi-chamber PECVD equipment for thin-film silicon layers deposition. Rear side layers consist of (*i*)/(*n*)a-Si:H layers stack deposited according to previous studies,[35–37] and same deposition conditions were used for all the samples within this work. Subsequently, (*i*)a-Si:H layer was deposited on the front side of the samples. In order to control the growth of high quality MoO_x thin films by achieving an optimal oxygen content, different (*i*)a-Si:H/MoO_x interface treatments were

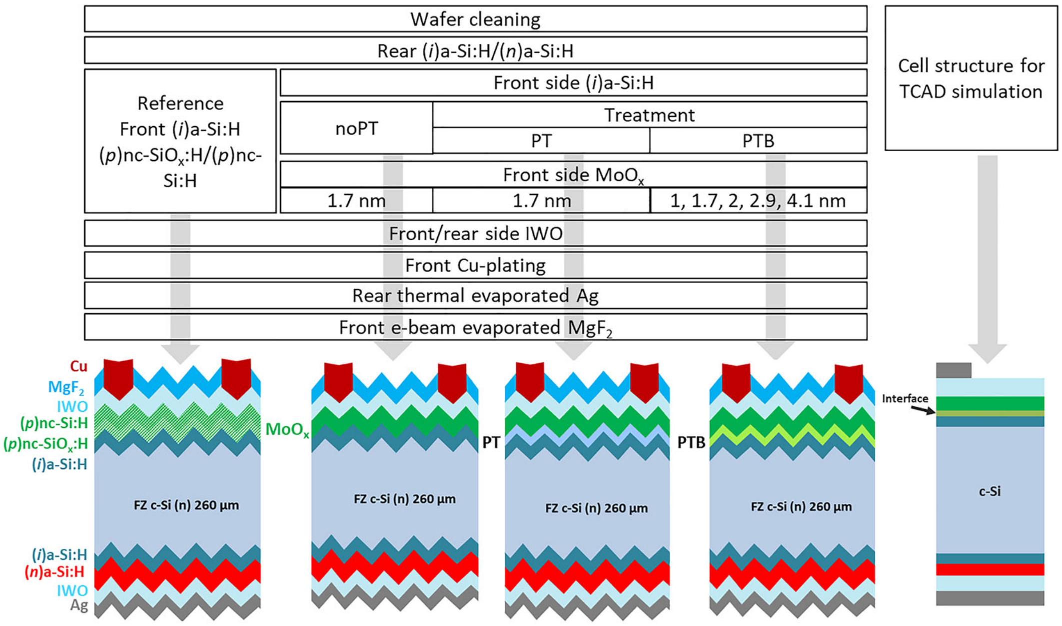

FIGURE 1 Flow chart of solar cells fabrication and cross-sectional sketches of the studied devices [Colour figure can be viewed at wileyonlinelibrary.com]

employed to investigate their effect on MoO_x properties. Accordingly, two different conditions were adopted after depositing (*i*)a-Si:H: using a highly hydrogen diluted (~170 sccm) gas mixture of (1) SiH_4, H_2 and CO_2, namely, PT (Plasma Treatment), or (2) SiH_4, H_2, CO_2 and B_2H_6, namely, PTB (Plasma Treatment with Boron radicals).[19] The inclusion of boron is optimal for deposition MoO_x as successfully demonstrated in our previous work.[19] As it will be shown in Section 3.3, these plasma treatments introduce two layers on top of porous (*i*)a-Si:H consisting of a-SiO_x:H/a-Si:H. PT and PTB processes used the same pressure (2.2 mbar) but different power density (76 and 90 mW/cm^2, respectively). Note that we also fabricated a sample without plasma treatment (noPT). Then, MoO_x layers were thermally evaporated at a base pressure of 5×10^{-6} mbar from a stoichiometric MoO_3 powder source at a deposition rate of about 0.1 nm/s. We used a reference front-junction SHJ sample for comparison purposes featuring 21-nm-thick p-layer as reported elsewhere.[38] After that, optimized 50- and 150-nm-thick tungsten-doped indium oxide (IWO) layers were sputtered through a hard mask at front and rear side, respectively, defining six 2×2 cm^2 solar cells per wafer.[39] The front metal electrode consists of electroplated Cu fingers at room temperature on top of 200-nm-thick thermally evaporated Ag seed layer.[40,41] The rear metal electrode was formed by 500-nm-thick thermally evaporated Ag. Finally, 100-nm-thick MgF_2 was e-beam evaporated on the front side as an additional antireflection coating layer. All abovementioned layer thickness were calculated from the nominal thickness applying the geometrical factor of 1.7 for a textured surface.[42]

Effective minority carrier lifetimes were measured at different steps of the fabrication by Sinton-120 equipment. Current–voltage characteristics of solar cells were determined using an AAA-rated Wacom WXS-90S-L2 solar simulator under standard test conditions. In-house external quantum efficiency (EQE) equipment, operated with photodiode calibrated at Fraunhofer ISE, was employed to obtain the $J_{sc,EQE.}$ Measuring the spectral response was performed on a dedicated cell without metal grid. Compositional investigation of MoO_x layers was carried out with a ThermoFisher K-Alpha X-ray photoelectron spectrometer (XPS).[43,44] The XPS uses an Al Kα X-ray source with an energy of 1486.68 eV. The base pressure of the processing chamber is 2×10^{-9} mbar. The measurement was carried out at room temperature after the high vacuum was obtained. Note that samples for XPS analysis were prepared using 280 ± 20 μm flat <111> n-type float-zone (FZ) wafers with the identical processes as reported in Figure 1 to mimic the same surface orientation available at the pyramid facets in solar cells and adapting the deposition time to achieve the same thicknesses as in textured samples. High-resolution transmission electron microscope (HR-TEM) combined with energy dispersive X-Ray spectroscopy (EDX) was employed to evaluate the structure and composition of the contact stack on lamellas taken from solar cells with higher performance (i.e., cells endowed with 1.7-nm-thick MoO_x layers). Finally, contact resistivity (ρ_c) of the contact stack was measured in samples using double textured p-type <100> FZ wafers (260 ± 20-μm-thick after texturing).[38] The schematic structure of these stacks of layers can be found in Figure S1.

2.2 | Simulations

We investigated the atomistic phenomena at the Si/MoO_x interface by means of first-principle density functional theory (DFT) calculations via *Vienna* Ab initio *Simulation Package* (VASP). We analyzed the thermodynamically stable orthorhombic α-phase of molybdenum trioxide. α-MoO_3 crystallizes with four formula units of MoO_3 in an orthorhombic cell with symmetry Pbnm.[45] This makes the unit cell to be composed of 4 Mo atoms and 12 O atoms, with lattice constants a = 3.96 Å, b = 13.85 Å, and c = 3.70 Å. The structure of molybdenum oxide is based on bilayers oriented perpendicular to the y axis fastened across that axis by weak van der Waals forces. Each bilayer consists of two sublayers of distorted MoO_6 octahedra that form edge-sharing zigzag rows along the z direction and corner sharing rows along the x direction.[46] These internal interactions are held by strong covalent and ionic bonds. For silicon, we considered crystals in a cubic diamond structure with a lattice constant of 5.43 Å,[47] corresponding to the Fd3m space group.[48] Its structure can be seen as two interpenetrating face centered cubic sublattices with one sublattice displaced from the other by one-quarter of the distance along the body diagonal of the cube.[49] All Si atoms are bonded to four equidistant neighbors to form a tetrahedron. Accordingly, Si is simulated in combination with α-MoO_3 to mimic the interface between the two materials, based on the Perdew-Burke-Ernzerhof (PBE) functional. We then calculated the WF of MoO_x structures as the difference between the vacuum potential and the Fermi energy.[50] For the calculation of the dipole formed at Si/MoO_x interface, we used the lattice coincidence method.[51]

Electrical simulations of SHJ solar cells were carried out using TCAD Sentaurus.[52] The input optical generation profile was obtained by raytracing simulations executed in GenPro4.[53] Therefore, a two-dimensional domain of the solar cell (Figure 1) is considered for the solution of drift-diffusion equations consistently coupled with charge transport models at heterointerfaces. We accounted models and parameters reported in other works[54,55] for c-Si and thin-film silicon. Note that in TCAD we took into consideration a virtual layer to mimic the interface phenomena resulted from DFT simulations (i.e., dipole formation).[19,56]

3 | RESULTS AND DISCUSSION

3.1 | Significance of Si/MoO_x interface

Electronic properties of MoO_x strongly depend on the oxidation states.[29] Moreover, by controlling the oxidation–reduction reaction between a substrate and MoO_x, it is possible to adjust the WF of $MoO_{x.}$[29] Accordingly, we theoretically evaluate the Si/MoO_x interface.[51] Figure 2A reports the differential charge as function of the position after the formation of such interface for different oxygen content in MoO_x (x in MoO_x) from 3 to 2.875. The curves indicate the charge variation due to the interaction between the two adjacent materials. We observe that there is an interface region, which does not accomplish the lattice conditions for Si or MoO_x materials. Such a

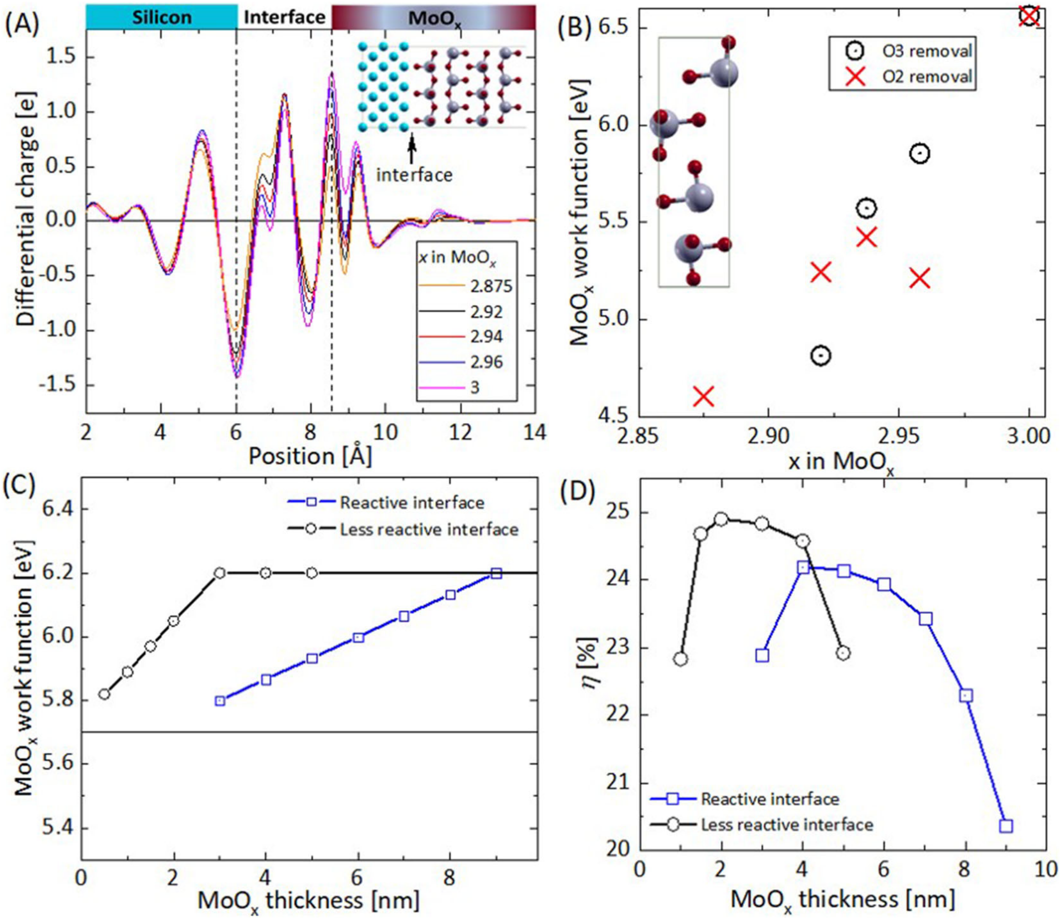

FIGURE 2 (A) Differential charge at the interface between Si and MoO$_x$ for different stoichiometry in MoO$_x$. The inset depicts the cross-sectional view of the Si/MoO$_x$ interface and the arrow indicates the 2.5-Å-thick interface in which the dipole forms (silicon is represented by light blue atoms while MoO$_x$ is represented by gray atoms for Mo and red atoms for oxygen). (B) Calculated work functions of MoO$_x$ as a function of x in MoO$_x$ for different oxygen deficiencies: O3 and O2 removal. The inset depicts the unit cell of MoO$_3$ as modelled in DFT simulations. (C) Work function profile used to emulate different (*i*)a-Si:H/MoO$_x$ interfaces: reactive (blue squares) and less reactive (black circles). (D) Simulated conversion efficiency (η) of SHJ with MoO$_x$ hole collector using WF profiles taken from (C) as input. Simulated J_{sc}, V_{oc}, and FF are shown in Figure S2. [Colour figure can be viewed at wileyonlinelibrary.com]

region exhibits differential charge variation due to interaction between Si and O atoms forming the Si-O bonds at the interface between Si and MoO$_x$. Interestingly, we observe that the largest peaks are at the edge of Si lattice (6 Å) and MoO$_x$ lattice (8.5 Å). Such peaks exhibit similar magnitudes but opposite charge fulfilling the conditions to form a dipole.[57] Eventually, the dipole implies potential drops across the interface attenuating the WF of MoO$_x$. The magnitude of such dipole decreases for lower oxygen content in MoO$_x$ as shown in the Table S1. We then calculate the WF of MoO$_x$ for different x by simulating different oxygen deficiencies, that is removing O3 or O2 states. Figure 2B shows that the WF strongly increases as x in MoO$_x$ gets closer to 3. In fact, we observe a 2 eV rise in WF when x in MoO$_x$ changes from 2.85 to 3. Looking at experimental evidence in literature, it is worth noting that the oxygen state of MoO$_x$ depends on oxidation potential of the adjacent layer[58] and deposition conditions.[59] In addition, although the thickness of MoO$_x$ does not directly denote its oxidation state, there is a clear correlation between layer thickness and x in MoO$_x$, for which the thicker the MoO$_x$ layer is, the more stoichiometric the resulting material is. This was experimentally observed in MoO$_x$ deposited on different substrates as reported.[29]

In this work, we are specifically interested in the (*i*)a-Si:H/MoO$_x$ interface. Ideally, given the abovementioned dependencies, a MoO$_x$ film should straightaway exhibit a certain WF value (anywhere between 5.8 and 7 eV)[60–63] as long as the dipole is formed between the MoO$_x$ film and its substrate. That is, a step-like function for WF as function of MoO$_x$ thickness should be ideally established (WF = 0 for thickness ~0 nm and WF = constant for thickness >0 nm). However, this is not what happens as the MoO$_x$ material grows on a substrate. The approach reported in[19] links the dependence of MoO$_x$ WF on its thickness to the (*i*)a-Si:H WF, the built-in potential at the (*i*)a-Si:H/MoO$_x$ interface and the attenuation of MoO$_x$ WF due to the presence of the abovementioned dipole. Based on that approach, we expect that the dependency of MoO$_x$ WF on its thickness reaches a saturation value which depends on (i) the deposition process, (ii) the growth condition of MoO$_x$ and (iii) the reactivity of the substrate with oxygen states. In case of silicon substrate, silicon indeed reacts with the oxygen

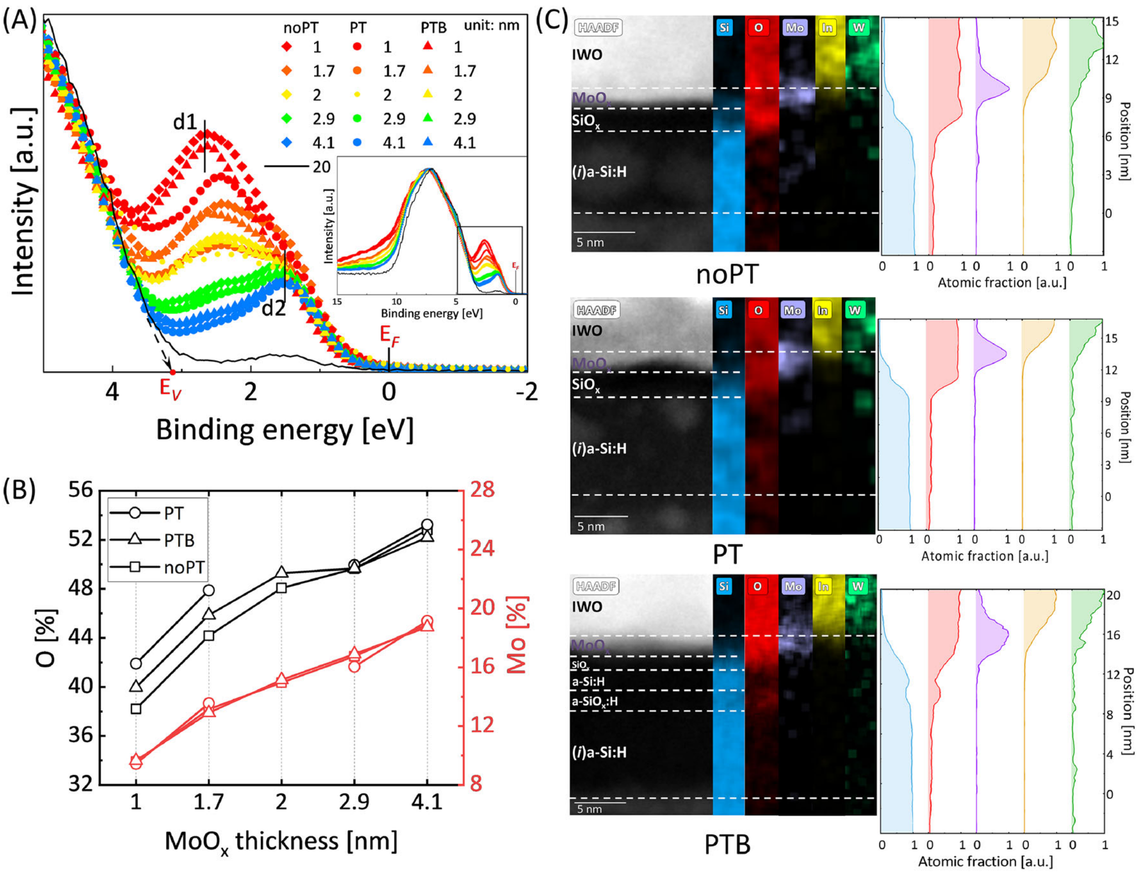

FIGURE 3 (A) Valence band spectra of as-deposited MoO$_x$ surface for variable thicknesses and noPT, PTB, and PT. d1 and d2 indicate the gap states caused by O vacancies (the inset zooms out these spectra in a wider binding energy range); (B) the Mo and O content as a function of MoO$_x$ thickness under different treatment calculated from XPS spectra (see Figures S3 and S4); (C) EDX images of noPT sample (top), PT sample (middle), and PTB sample (bottom) [Colour figure can be viewed at wileyonlinelibrary.com]

diffused from MoO$_x$, leading to the formation of a thin SiO$_x$ layer film at Si/MoO$_x$ interface.[58] We illustrate this concept in Figure 2C, where a *less reactive* interface prior to the MoO$_x$ deposition would saturate the WF within a 3-nm-thick MoO$_x$ films,[58] while a *reactive* interface would achieve similar WF only for 9-nm-thick MoO$_x$ films.[19] The reported trend of the less reactive interface is one of the several possibilities that could be experimentally feasible between the reactive interface case on the one hand and the previously mentioned ideal WF step function on the other hand. We chose that specific trend with its saturated WF value at 6.2 eV because, once used in our TCAD-based simulation campaign to validate our simulation framework, it could explain well both our experimental trends as well as those in other works.[19,25]

So, to evaluate the effect of different (*i*)a-Si:H interface conditions on SHJ solar cell performance, we performed TCAD simulations accounting for these two different WF profiles. After considering the interface dipole and SiO$_x$ formation as[19] we obtained the conversion efficiency (η) trends reported in Figure 2D as function of the MoO$_x$ thickness. The simulated *FF*, J_{sc} and V_{oc} trends are provided in Figure S2. We observe a bell-shaped η, which is dominated by the *FF* trend as shown in Figure S2 and discussed.[19] The trend of η demonstrates a maximum value of 24.2% and 24.9% at around 4 and 2 nm MoO$_x$ for reactive and less reactive WF profiles, respectively. Maximum values in each curve result indeed from the trade-off between WF and interfacial dipole.[19] The interfacial dipole leads to an attenuation of MoO$_x$ WF. Accordingly, increasing MoO$_x$ thickness amplifies WF but also the WF attenuation. Note that WF attenuation has a negative impact on the c-Si band bending and energy alignment within c-Si/(*i*)a-Si:H/TCO and thus affects the *FF* of solar cells as discussed.[19] It is possible to achieve the best trade-off between WF and WF attenuation with thinner MoO$_x$ in case of a less reactive surface. We observe that the highest η of 24.9% is achieved by means of a less reactive interface and for 2-nm-thick MoO$_x$. Indeed, interfaces that are less reactive with oxygen have the potential to improve η and minimize the MoO$_x$ layer thickness. To mitigate such oxygen reactivity with silicon molecules and therefore to control MoO$_x$ WF and dipole formation at Si/MoO$_x$ interface, we then proposed[19] the approach to modify the interface before MoO$_x$ deposition by applying a PECVD plasma treatment on top of (*i*)a-Si:H layer.

3.2 | Modification of (*i*)a-Si:H to control the properties of MoO$_x$

We used two different plasma treatments (PT and PTB) to modify (*i*)a-Si:H before MoO$_x$ deposition as described in Section 2.1. Accordingly, we evaluate the oxygen (O) vacancies in MoO_x films for three different interface conditions: noPT, PT, and PTB. Among these interface conditions, we also evaluate oxygen vacancies in samples with different MoO_x thickness: 1, 1.7, 2, 2.9, and 4.1 nm. Additionally, we included a 20-nm-thick MoO_x sample as reference. Then, we conducted XPS to evaluate the elemental composition of these samples. Figure 3A shows the valence band photoemission spectra of MoO_x. We relate this parameter with the gap states between the Fermi level and valence band,[29] and they are indicated as d1 and d2. The idle oxidation state of Mo is +6, corresponding to MoO_3 (Figure S2). Instead, the gap states are the dominant defect resulting in degradation of Mo cation state from +6 to +5.[30,64] In general, we observe that (i) samples with noPT show the highest gap states concentration and (ii) the gap states signal decreases for samples with thicker MoO_x layer. Note that the 20-nm-thick MoO_x sample exhibits almost no signal of gap states. This is consistent with observation from Mo core-level spectra as shown in Figure S2. In fact, according to the Mo core-level spectra, we confirm the presence of different Mo oxidation states (Mo^{+6} and Mo^{+5}) in different MoO_x-thickness films. These results are in agreement with observations reported in[44] by evaluating Mo oxidation states in MoO_x layers grown onto different reactive substrates.[58] As the Mo^{+5} decreases when the thickness of MoO_x film increases, we can correlate such a reduction to an increase in MoO_x WF. Thus, we expect a rise in the WF for thicker MoO_x samples.[13,18] We notice that all three interface conditions (noPT, PT, and PTB) show a similar trend. Also, we see that gap states signal is lower for PT than PTB and noPT in case of samples with MoO_x layer thinner than 2.9 nm. Figure 3B shows the O and Mo content calculated from XPS as a function of the thickness of MoO_x samples. In particular, the atomic concentrations of O and Mo under three conditions and for 1- and 1.7-nm-thick MoO_x are provided in Table S2. In general, we observe that molybdenum content remains the same independently of the interface condition. However, the O content increases with the layer thickness for the three different treatments. We noted that O content is the lowest for noPT samples, which indicates that MoO_x layers are less stoichiometric compared with PTB and PT cases. MoO_x samples treated with PT exhibit higher oxygen content. This trend is observed systematically up to 2.9 nm; after this value, the effect of PT or PTB is not detectable. This suggests that noPT samples exhibit interface features allowing oxygen to diffuse from MoO_x. Instead, PTB and PT processes modify the interface preventing the oxygen diffusion from the MoO_x layer. Moreover, looking at the oxygen content of MoO_x films and its relation to the WF reported in[65] we expect that samples with PT provide the highest WF followed by those with PTB and noPT.

3.3 | The role of oxygen at (*i*)a-Si:H/MoO_x interface

To evaluate the element composition and the morphology of the (*i*)a-Si:H/MoO_x interface, we conducted HR-TEM and EDX measurements for solar cells fabricated under different interface conditions (i.e., noPT, PT and PTB) with nominal 1.7-nm-thick MoO_x layer and including the IWO as TCO layer. As this thickness yields the best performing solar cells (see Section 3.4), it was chosen for this evaluation. Figure 3C shows the EDX map and the element composition profile of Si, O, Mo, In and W. The origin of depth profiling analysis was set at the interface between c-Si bulk and the (i)a-Si:H layer (see detailed cross-sectional TEM images in Figure S3 and EDX raw data in Figure S7). Note also that we evaluate the thickness of each (sub)layer in Figure S3.

We observe that samples with PT and PTB exhibit a thicker Si-rich layer than the sample with noPT. This suggests that PT and PTB form on the original (*i*)a-Si:H layer, an interlayer with different interface conditions with respect to the sample with noPT. In case of PT, as observed in[66] too, we speculate that oxygen radicals do not incorporate in film incubation phase (~2 nm) under the aforementioned plasma processing conditions. In case of PTB, the presence of boron radicals in the plasma leads to faster reaction[67] with oxygen atoms that are incorporated in the film nucleation phase. In this scenario, boron atoms act no longer as a dopant[68] but as oxidation agent. This is consistent with XPS and TEM measurements in which boron cannot be detected (see Figures S6 and S7). For the noPT sample, we note in both Figures 3C and S4 that oxygen is extended inside (*i*)a-Si:H forming an oxygen-rich interlayer at (*i*)a-Si:H/MoO_x interface. We ascribe the origin of such a sub-layer to the O diffusion from MoO_x to the interface resulting in 2.2 nm SiO_x interlayer. The MoO_x thickness mentioned later was calculated from the Mo and In atomic profiles, because these two atomic distributions have clear boundaries as shown in Figure 3C. The overlap area in the Mo and In atomic profile are ascribed to the intermixing layer[16] formed during IWO-sputtering process. In this sample, we observe the formation of ~2-nm-thick MoO_x layer. In the sample with PT, we note instead the formation of 2-nm-thick SiO_x interlayer and a ~2-nm-thick MoO_x film. The sample with PTB exhibits the formation of a thinner SiO_x interlayer (1 nm) at (*i*)a-Si:H/MoO_x interface and ~2.2-nm-thick MoO_x film. However, there is an additional 1.5-nm-thick a-Si:H and 1.8-nm a-SiO_x:H layer above (*i*)a-Si:H formed during PTB. The atomic fraction of O, Si, and Mo of such interlayers is shown in Figure 3C. As mentioned earlier, we note that Mo diffuses also inside IWO (W-rich) layer for all samples, for which the element profiles of Mo, O, and In (see Figure 3C) reveal the formation of a transition interlayer at the MoO_x/IWO interface. We suppose the mixing layer is formed during the IWO deposition process due to the sputtering process. These observations are consistent with findings reported in Geissbühler et al.[16] Ultimately, our elemental process indicates that the MoO_x layer is affected by two main interfaces—(*i*)-a-Si:H/MoO_x and MoO_x/IWO—that concurrently affect the electronic properties of MoO_x.

3.4 | Solar cells' performance

Finally, we evaluate the solar cell parameters using the nominal 1.7-nm-thick MoO_x layer with different interface treatments (noPT, PT and PTB). The external parameters are reported in Figure 4A. We

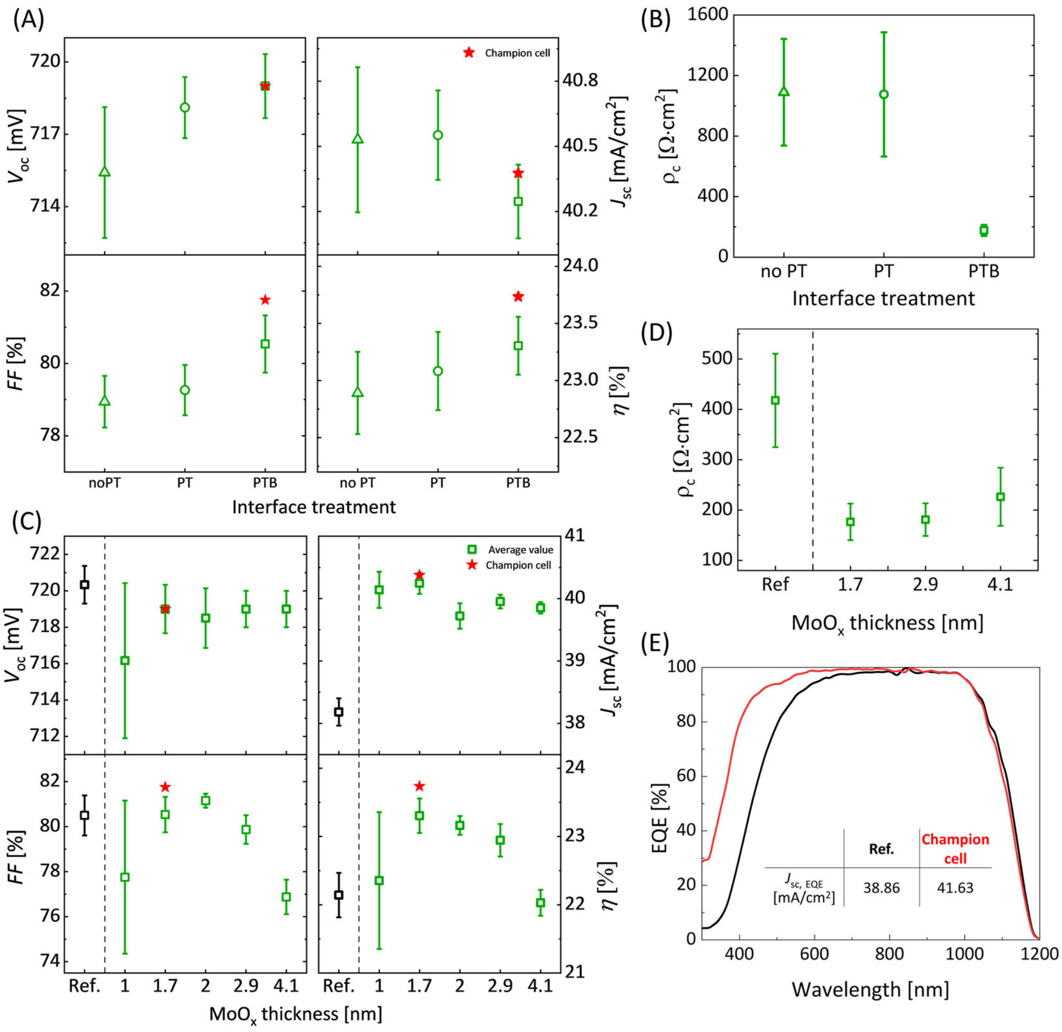

	Ref.	Champion cell
$J_{sc,\,EQE}$ [mA/cm^2]	38.86	41.63

FIGURE 4 (A) The parameters extracted from J-V curve of solar cells with various interface treatments at 1.7-nm-thick MoO$_x$ (the error bar is calculated from 12 solar cells on 4 wafers for noPT, 9 solar cells on 3 wafers for PT and 18 solar cells on 6 wafers for PTB); (B) contact resistivity of different treatments applied before depositing 1.7-nm-thick MoO$_x$ (six samples for each condition); (C) the parameters extracted from J-V curve of solar cells with PTB and various MoO$_x$-thickness (the error bar is calculated from 6 solar cells on 2 wafers for Ref., 1 nm and 2 nm cases; from 3 solar cells on 1 wafer for 2.9 and 4.1 nm cases; from 18 solar cells on 6 wafers for 1.7 nm case); (D) contact resistivity of different MoO$_x$ thickness with PTB, including a p-type layer as reference (6 samples for each condition). (The empty symbols stand for the standard average value and the standard error bar is calculated from multiple samples; the red star symbol represents the external parameters of the champion cell); (E) EQE spectra of the reference SHJ solar cell and champion MoO$_x$ solar cell. [Colour figure can be viewed at wileyonlinelibrary.com]

observe that V_{OC} and *FF* exhibit the highest (719 mV, 80.66%) and lowest (715 mV, 79.16%) for samples with PTB and noPT, respectively. This result is consistent with ρ_c values reported in Figure 4B and with findings in Tong et al.[33] In fact, we observe the lowest ρ_c value of 177 mΩ cm^2 for sample with PTB. NoPT and PT result in ρ_c in the range of 600 to 1400 mΩ cm^2. We can relate that a-Si:H and a-SiO$_x$:H interlayer formation during PTB process, together with higher oxygen content in MoO$_x$ layer, leads to transport improvement in the contact stack with PTB. We infer that samples with PT MoO$_x$ could exhibit higher WF than samples using PTB due to the higher oxygen content (Figure 3B). However, we suspect that PTB samples result in the lowest ρ_c due to the best trade-off between WF and interfacial dipole.[19] Samples with noPT exhibit high ρ_c due to high oxygen reaction at (*i*)a-Si:H/MoO$_x$ interface together with lower oxygen content in MoO$_x$ (relatively low MoO$_x$ WF) as discussed in the previous section.

We note that the trend is opposite for short circuit current (J_{sc}) as Figure 4A illustrates. The samples without any treatment (noPT) yield the highest J_{sc}. This is ascribed to the fact that interface modification (i.e., PT and PTB) leads to the growth of ∼3-nm-thick interlayer (see Section 3.3), which increases the parasitic absorption in samples with PT and PTB. Such interlayer causes J_{sc} losses of 0.2–0.4 mA/cm^2 compared to samples with noPT. Note that XPS and EDX measurements show that PTB does not result in boron incorporation. In general, η follows the trend of V_{OC} and *FF* with highest value of 23.83% for samples with PTB.

As PTB solar cells exhibit the highest efficiency in our study (Figure 4A), we evaluate the effect of MoO$_x$ thickness for such

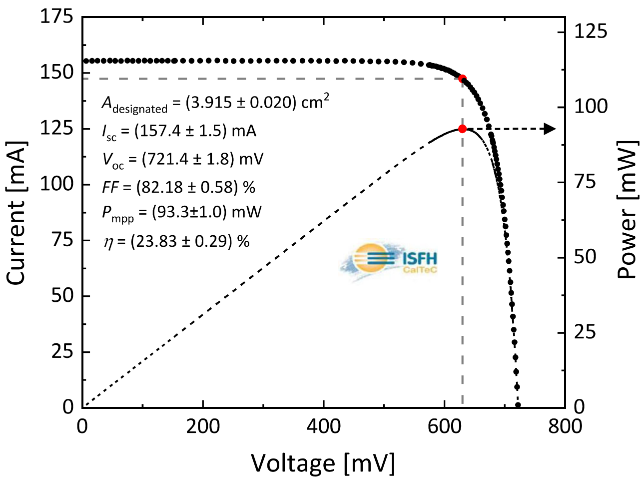

FIGURE 5 ISFH CalTeC certified J-V and P-V curves of our champion cell based on 1.7-nm-thick MoO_x and PTB [Colour figure can be viewed at wileyonlinelibrary.com]

treatment. Solar cell performance of devices fabricated with noPT for variable MoO_x thickness was investigated in the early development of this method. Related results reported in our previous work[19] were not encouraging. To do so, we variate the MoO_x layer from 1 to 4 nm. The results are reported in Figure 4C. V_{OC} of the devices increases as the thickness of MoO_x reaches 1.7 nm and remains constant at around 719 mV for samples with MoO_x thicker than 1.7 nm. *FF* exhibits a bell-shape trend with a maximum average value of around 81.5% for 2-nm-thick MoO_x. This trend is consistent with theoretical findings in Section 3.1 and ρ_c measurements reported in Figure 4D.

As anticipated, increasing MoO_x thickness, J_{sc} slightly decreases from 40.2 to 39.8 mA/cm^2 due to parasitic absorption. Furthermore, the EQE of the best MoO_x cell compared to the SHJ counterpart is shown in Figure 4E. We observe that the EQE spectrum exhibits an improvement in light response at wavelength range from 300 to 800 nm corresponding to a gain of 2.77 mA/cm^2. We observe that the η trend is dominated by the *FF*. Indeed, the best trade-off between optics and electrical behavior (J_{SC} vs FF^*V_{oc}) results in an optimal solar cell with 1.7 nm MoO_x. Figure 5 shows the certified J-V curve of our best performing solar cell.

4 | CONCLUSION

In this work, we identified the fundamental mechanisms for tailoring properties of MoO_x and for its integration in high-efficiency SHJ solar cells. Our simulation results revealed that the oxygen content inside MoO_x strongly affects the WF and additionally leads to the formation of a strong dipole at the interface with silicon. Therefore, thickness dependent WF profile depends on the diffusion of oxygen from MoO_x through (*i*)a-Si:H. Then, by controlling the oxygen content in MoO_x, we calculated that optimal solar cells are possible for $\sim$2-nm-thick ultra-thin MoO_x films because of the trade-off between dipole and MoO_x WF. With this observation, we investigated the effect of PT and PTB on MoO_x film oxygen content. By evaluating XPS measurements, we observed that oxygen content in MoO_x layers deposited after PT and PTB conditions is higher than that in MoO_x layers deposited in noPT condition. This finding suggests adjustable WF for PT and PTB samples as WF increases with oxygen content in MoO_x. HR-TEM and EDX images confirmed the formation of a SiO_x interlayer at (*i*)a-Si:H/MoO_x interface. We noted that samples with PT and PTB exhibited thinner SiO_x interlayer compared with samples with noPT, thus confirming that PT and PTB indeed reduce the reaction of the (*i*) a-Si:H/MoO_x interface with oxygen from MoO_x. We evaluated the transport of the contact stack in terms of ρ_c of samples with noPT, PT and PTB. Our measurements revealed a minimal $\rho_c = 177$ mΩ cm^2 for a contact stack with PTB and 1.7 nm MoO_x. Then, we studied the impact of the interface treatment and MoO_x-thickness on the performance of MoO_x-based SHJ solar cells. Overall, we applied optimal PTB at (*i*)a-Si:H/MoO_x interface and realized a champion cell with 1.7-nm (2.2-nm measured by TEM) thick MoO_x as a hole transport layer. With 23.83% conversion efficiency and a *FF* equal to 82.18%, we push further the performance of TMO materials integrated in c-Si solar cell architectures. Furthermore, plasma processes applied here (PT and PTB) for reaching high performance solar cells are compatible with industry SHJ production lines.

ACKNOWLEDGEMENTS

This work was supported by the project Momentum (TKITOE1821101), which receives funding from the Topsector Energie of the Dutch Ministry of Economic Affairs and Climate Policy. The authors thank Martijn Tijssen and Stefaan Heirman for their technical support and Bart Boshuizen for discussion on XPS analysis. Liqi Cao would like to thank China Scholarship Council (CSC NO. 202006740021) for the financial support.

DATA AVAILABILITY STATEMENT

The data that support the findings of this study are available from the corresponding author upon reasonable request.

ORCID

Liqi Cao https://orcid.org/0000-0001-8076-6249
Paul Procel https://orcid.org/0000-0003-4997-3551
Yifeng Zhao https://orcid.org/0000-0003-3789-5090
Can Han https://orcid.org/0000-0002-3213-6856

REFERENCES

1. Ballif C, Haug FJ, Boccard M, Verlinden PJ, Hahn G. Status and perspectives of crystalline silicon photovoltaics in research and industry. *Nat Rev Mater*. 2022;0123456789(8):597-616. doi:10.1038/s41578-022-00423-2
2. Haschke J, Dupré O, Boccard M, Ballif C. Silicon heterojunction solar cells: recent technological development and practical aspects - from lab to industry. *Sol Energy Mater sol Cells*. 2018;187(July):140-153. doi:10.1016/j.solmat.2018.07.018
3. LONGI Solar, LONGi once again sets new world record for HJT solar, 2022, [Online]. Available: https://www.longi.com/en/news/new-hjt-world-record/.

4. Holman ZC, Descoeudres A, Barraud L, et al. Current losses at the front of silicon heterojunction Solar cells. *IEEE J Photovoltaics*. 2012;2(1):7-15. doi:10.1109/JPHOTOV.2011.2174967
5. Shi J, Shen L, Liu Y, et al. MoOx modified ITO/a-Si:H(p) contact for silicon heterojunction solar cell application. *Mater Res Bull*. 2018;97:176-181. doi:10.1016/j.materresbull.2017.09.005
6. Peter Seif J, Descoeudres A, Filipič M, et al. Amorphous silicon oxide window layers for high-efficiency silicon heterojunction solar cells. *J Appl Phys*. 2014;115(2):024502. doi:10.1063/1.4861404
7. Bullock J, Wan Y, Hettick M, et al. Dopant-free partial rear contacts enabling 23% silicon Solar cells. *Adv Energy Mater*. 2019;9(9):1-6. doi:10.1002/aenm.201803367
8. Yang X, Aydin E, Xu H, et al. Tantalum nitride Electron-selective contact for crystalline silicon Solar cells. *Adv Energy Mater*. 2018;8(20):1-7. doi:10.1002/aenm.201800608
9. Yang X, Bi Q, Ali H, Davis K, Schoenfeld WV, Weber K. High-performance TiO2-based Electron-selective contacts for crystalline silicon Solar cells. *Adv Mater*. 2016;28(28):5891-5897. doi:10.1002/adma.201600926
10. Bullock J, Wan Y, Xu Z, et al. Stable dopant-free asymmetric Heterocontact silicon Solar cells with efficiencies above 20%. *ACS Energy Lett*. 2018;3(3):508-513. doi:10.1021/acsenergylett.7b01279
11. Lin W, Wu W, Liu Z, et al. Chromium trioxide hole-selective Heterocontacts for silicon Solar cells. *ACS Appl Mater Interfaces*. 2018;10(16):13645-13651. doi:10.1021/acsami.8b02878
12. Bivour M, Temmler J, Steinkemper H, Hermle M. Molybdenum and tungsten oxide: high work function wide band gap contact materials for hole selective contacts of silicon solar cells. *Sol. Energy Mater. Sol. Cells*. 2015;142:34-41. doi:10.1016/j.solmat.2015.05.031
13. Gerling LG, Voz C, Alcubilla R, Puigdollers J. Origin of passivation in hole-selective transition metal oxides for crystalline silicon heterojunction solar cells. *J Mater Res*. 2017;32(2):260-268. doi:10.1557/jmr.2016.453
14. Gao P, Yang Z, He J, et al. Dopant-Free and Carrier-Selective Heterocontacts for Silicon Solar Cells: Recent Advances and Perspectives. *Adv Sci*. 2018;5(3):1700547. doi:10.1002/advs.201700547
15. Bullock J, Hettick M, Geissbühler J, et al. Efficient silicon solar cells with dopant-free asymmetric heterocontacts. *Nat Energy* 2016;1(3):15031. doi:10.1038/nenergy.2015.31
16. Geissbühler J, Werner J, Martin de Nicolas S, et al. 22.5% efficient silicon heterojunction Solar cell with molybdenum oxide hole collector. *Appl Phys Lett*. 2015;107(8):081601. doi:10.1063/1.4928747
17. Bullock J, Cuevas A, Allen T, Battaglia C. Molybdenum oxide MoOx: a versatile hole contact for silicon solar cells. *Appl Phys Lett*. 2014;105(23):232109. doi:10.1063/1.4903467
18. Ali H, Koul S, Gregory G, et al. In situ transmission Electron microscopy study of molybdenum oxide contacts for silicon Solar cells. *Phys Status Solidi Appl Mater Sci*. 2019;216(7):1-4. doi:10.1002/pssa.201800998
19. Mazzarella L, Alcañiz A, Procel P, et al. Strategy to mitigate the dipole interfacial states in (i)a-Si:H/MoOx passivating contacts solar cells. *Prog. Photovoltaics Res. Appl*. 2021;29(3):391-400. doi:10.1002/pip.3381
20. Jasieniak JJ, Seifter J, Jo J, Mates T, Heeger AJ. A solution-processed MoO x anode interlayer for use within organic photovoltaic devices. *Adv Funct Mater*. 2012;22(12):2594-2605. doi:10.1002/adfm.201102622
21. Macco B, Vos MFJ, Thissen NFW, Bol AA, Kessels WMM. Low-temperature atomic layer deposition of MoOx for silicon heterojunction solar cells. *Phys Status Solidi - Rapid Res Lett*. 2015;9(7):393-396. doi:10.1002/pssr.201510117
22. Tong J, Wan Y, Cui J, Lim S, Song N, Lennon A. Solution-processed molybdenum oxide for hole-selective contacts on crystalline silicon solar cells. *Appl Surf Sci*. 2017;423:139-146. doi:10.1016/j.apsusc.2017.06.011
23. Pan T, Li J, Lin Y, et al. Structural and optical studies of molybdenum oxides thin films obtained by thermal evaporation and atomic layer deposition methods for photovoltaic application. *J Mater Sci Mater Electron*. 2021;32(3):3475-3486. doi:10.1007/s10854-020-05094-9
24. Wang F, Zhao S, Liu B, et al. Silicon solar cells with bifacial metal oxides carrier selective layers. *Nano Energy*. 2017;39(July):437-443. doi:10.1016/j.nanoen.2017.07.014
25. Dréon J, Jeangros Q, Cattin J, et al. 23.5%-efficient silicon heterojunction silicon solar cell using molybdenum oxide as hole-selective contact, *Nano Energy*. 2020:104495. doi:10.1016/j.nanoen.2020.104495
26. Neusel L, Bivour M, Hermle M. Selectivity issues of MoOx based hole contacts. *Energy Procedia*. 2017;124:425-434. doi:10.1016/j.egypro.2017.09.268
27. Zhang T, Lee C-Y, Wang Y, Lim S, Hoex B. Investigation of the thermal stability of MoOx as hole-selective contacts for Si solar cells. *J Appl Phys*. 2018;124(7):073106. doi:10.1063/1.5041774
28. Cho J, Nawal N, Hadipour A, et al. Interface analysis and intrinsic thermal stability of MoOx based hole-selective contacts for silicon heterojunction solar cells. *Sol Energy Mater Sol Cells*. 2019;201:110074. doi:10.1016/j.solmat.2019.110074
29. Greiner MT, Chai L, Helander MG, Tang WM, Lu ZH. Metal/metal-oxide interfaces: how metal contacts affect the work function and band structure of MoO3. *Adv Funct Mater*. 2013;23(2):215-226. doi:10.1002/adfm.201200993
30. Greiner MT, Chai L, Helander MG, Tang WM, Lu ZH. Transition metal oxide work functions: the influence of cation oxidation state and oxygen vacancies. *Adv Funct Mater*. 2012;22(21):4557-4568. doi:10.1002/adfm.201200615
31. Sacchetto D, Jeangros Q, Christmann G, et al. ITO/MoOx/a-Si:H(i) hole-selective contacts for silicon heterojunction Solar cells: degradation mechanisms and cell integration, *IEEE J Photovoltaics*. 2017;7(6):1584-1590. doi:10.1109/JPHOTOV.2017.2756066
32. Cao S, Li J, Zhang J, et al. Stable MoOX-based Heterocontacts for p-type crystalline silicon Solar cells achieving 20% efficiency. *Adv Funct Mater*. 2020;30(49):1-9. doi:10.1002/adfm.202004367
33. Tong J, le TT, Liang W, et al. Impact of Pregrown SiOxon the carrier selectivity and thermal stability of molybdenum-oxide-passivated contact for Si Solar cells. *ACS Appl Mater Interfaces*. 2021;13(30):36426-36435. doi:10.1021/acsami.1c06765
34. Yang G, Han C, Procel P, et al. Oxygen-alloyed poly-Si passivating contacts for high-thermal budget c-Si heterojunction solar cells. *Prog Photovoltaics Res Appl*. 2022;30(2):141-151. doi:10.1002/pip.3472
35. Zhao Y, et al. Ultra-thin electron collectors based on nc-Si:H for high-efficiency silicon heterojunction solar cells. *Prog Photovoltaics Res Appl*. 2021;1-14. doi:10.1002/pip.3502
36. Zhao Y, Mazzarella L, Procel P, et al. Doped hydrogenated nanocrystalline silicon oxide layers for high-efficiency c-Si heterojunction solar cells. *Prog Photovoltaics Res Appl*. 2020;28(5):425-435. doi:10.1002/pip.3256
37. Zhao Y, Mazzarella L, Procel P, et al. Effects of (i) a-Si: H deposition temperature on high-efficiency silicon heterojunction solar cells. *Prog Photovoltaics Res Appl*. 2022;30(8):809-822. doi:10.1002/pip.3620
38. Zhao Y, Procel P, Han C., et al. Design and optimization of hole collectors based on nc-SiOx:H for high-efficiency silicon heterojunction solar cells. *Sol Energy Mater Sol Cells*. 2021;219:110779. doi:10.1016/j.solmat.2020.110779
39. Han C, Zhao Y, Mazzarella L, et al. Room-temperature sputtered tungsten-doped indium oxide for improved current in silicon heterojunction solar cells. *Sol Energy Mater Sol Cells*. 2021;227:111082. doi:10.1016/j.solmat.2021.111082
40. Limodio G, de Groot Y, van Kuler G, et al. Copper-plating metallization with alternative seed layers for c-Si Solar cells embedding carrier-selective passivating contacts. *IEEE J Photovoltaics*. 2020;10(2):372-382. doi:10.1109/JPHOTOV.2019.2957671

41. Han C, Yang G, Procel P, et al. Controllable simultaneous bifacial cu-plating for high efficiency crystalline silicon Solar cells. *Sol RRL*. 2022;6(6):2100810. doi:10.1002/solr.202100810
42. Özkol E, Wagner P, Ruske F, Stannowski B, Korte L. Optimization of Silicon Heterojunction Interface Passivation on p- and n-Type Wafers Using Optical Emission Spectroscopy, *Phys. Status Solidi Appl Mater Sci*. 2022;219(5). doi:10.1002/pssa.202100511
43. Scirè D, Procel P, Gulino A, Isabella O, Zeman M, Crupi I. Sub-gap defect density characterization of molybdenum oxide: an annealing study for solar cell applications. *Nano Res*. 2020;13(12):3416-3424. doi:10.1007/s12274-020-3029-9
44. Sun T, Wang R, Liu R, et al. Investigation of MoOx/n-Si strong inversion layer interfaces via dopant-free heterocontact. *Phys. Status Solidi - Rapid Res Lett*. 2017;11(7):1700107. doi:10.1002/pssr.201700107
45. Andersson G, Magneli A. On the crystal structure of molybdenum trioxide. *Acta Chem Scand*. 1950;4:793-797. doi:10.3891/acta.chem.scand.04-0793
46. de Castro IA, Datta RS, Ou JZ, et al. Molybdenum oxides – from fundamentals to functionality. *Adv Mater*. 2017;29(1701619):1-31. doi:10.1002/adma.201701619
47. Hom T, Kiszenik W, Post B. Accurate lattice constants from multiple reflection measurements. II. Lattice constants of germanium silicon, and diamond. *J Appl Cryst*. 1975;8(4):457-458. doi:10.1107/s0021889875010965
48. Neamen DA. *Semiconductor physics and devices basic principles*. Mc Graw Hill: Third; 2003.
49. Sze SM. *Semiconductor Devices - Physics and Technology*. 2008;
50. He C. Work function of (001) and (00-1) surface of α-Fe2O3. *Mod Phys Lett B*. 2018;32(17):1850188. doi:10.1142/S0217984918501889
51. Höffling B. The interfaces between silicon and transparent conducting oxides. *Friedrich-Schiller-Universität Jena*. 2015.
52. Synopsys, "TCAD Sentaurus: Sentaurus Device User Guide," *Version K-201506*, 2015.
53. Santbergen R, Meguro T, Suezaki T, Koizumi G, Yamamoto K, Zeman M. GenPro4 optical model for Solar cell simulation and its application to multijunction Solar cells. *IEEE J. Photovoltaics*. 2017;7(3):919-926. doi:10.1109/JPHOTOV.2017.2669640
54. Procel P, Xu H, Saez A, et al. The role of heterointerfaces and subgap energy states on transport mechanisms in silicon heterojunction solar cells. *Prog Photovoltaics Res Appl*. 2020;28(9):935-945. doi:10.1002/pip.3300
55. Procel P, Yang G, Isabella O, Zeman M. Theoretical evaluation of contact stack for high efficiency IBC-SHJ solar cells. *Sol Energy Mater Sol Cells*. 2018;186(May):66-77. doi:10.1016/j.solmat.2018.06.021
56. Würfel U, Seßler M, Unmüssig M, et al. How molecules with dipole moments enhance the selectivity of electrodes in organic Solar cells – a combined experimental and theoretical approach. *Adv Energy Mater*. 2016;6(19):1600594. doi:10.1002/aenm.201600594
57. Bisquert J. *Nanostructured energy devices: Equilibrium concepts and kinetics*. CRC Press; 2014. doi:10.1201/b17613
58. Greiner MT, Lu ZH. Thin-film metal oxides in organic semiconductor devices: Their electronic structures, work functions and interfaces, *NPG Asia Mater*. 2013;5(7). doi:10.1038/am.2013.29
59. Irfan I, Gao Y. Effects of exposure and air annealing on MoOx thin films. *J Photonics Energy*. 2012;2(1):021213. doi:10.1117/1.jpe.2.021213
60. Kumar M, Cho EC, Prodanov MF, Kang C, Srivastava AK, Yi J. MoOx work function, interface structure, and thermal stability analysis of ITO/MoOx/a-Si(i) stacks for hole-selective silicon heterojunction solar cells. *Appl Surf Sci*. 2021;553:149552. doi:10.1016/j.apsusc.2021.149552
61. Cauduro ALF, dos Reis R, Chen G, Schmid AK, Rubahn HG, Madsen M. Work function mapping of MoOx thin-films for application in electronic devices. *Ultramicroscopy*. 2017;183:1339-1351. doi:10.1016/j.ultramic.2017.03.025
62. Irfan I, Ding H, Gao Y, et al. Energy level evolution of air and oxygen exposed molybdenum trioxide films. *Appl Phys Lett*. 2010;96(24):10-13. doi:10.1063/1.3454779
63. Irfan I, James Turinske A, Bao Z, Gao Y. Work function recovery of air exposed molybdenum oxide thin films. *Appl Phys Lett*. 2012;101(9). doi:10.1063/1.4748978
64. Zhang Z, Xiao Y, Wei HX, et al. Impact of oxygen vacancy on energy-level alignment at MoOx/organic interfaces. *Appl Phys Express*. 2013;6(9). doi:10.7567/APEX.6.095701
65. He F, Yin X, Li J, et al. Characterization of sputtered MoOx thin films with different oxygen content and their application as back contact in CdTe solar cells, *Vacuum*. 2020;176:109337. doi:10.1016/j.vacuum.2020.109337
66. Mueller T, Ge J, Tang M, et al. Inductively coupled plasma deposited amorphous silicon alloys using industrial equipment for heterojunction silicon solar cells, in *2014 IEEE 40th photovoltaic specialist conference (PVSC)*. 2014;(i):0625-0628. doi:10.1109/PVSC.2014.6925000
67. Hand CW, Derr LK. Reaction of oxygen atoms with Diborane. *Inorg Chem*. 1974;13(2):339-342. doi:10.1021/ic50132a019
68. Terheiden B. CVD boron containing glasses - an attractive alternative diffusion source for high quality emitters and simplified processing - a review. *Energy Procedia*. 2016;92:486-492. doi:10.1016/j.egypro.2016.07.131

SUPPORTING INFORMATION

Additional supporting information can be found online in the Supporting Information section at the end of this article.

How to cite this article: Cao L, Procel P, Alcañiz A, et al. Achieving 23.83% conversion efficiency in silicon heterojunction solar cell with ultra-thin MoO_x hole collector layer via tailoring (*i*)a-Si:H/MoO_x interface. *Prog Photovolt Res Appl*. 2022;1-10. doi:10.1002/pip.3638